Exploiting Symmetries of FE Models and Application to Cohesive Elements

(3rd revised version)

Wolfgang Brocks[1], Diya Arafah[2], Mauro Madia[3]

Milano / Kiel, November 2013

[1] Christian-Albrechts-Universität, Kiel
[2] Politecnico di Milano
[3] Bundesanstalt für Materialforschung und -prüfung, Berlin

Abstract:

The present report provides information on the use of cohesive elements for the simulation of crack extension in specimens and structures with special focus on exploiting symmetry conditions. Applications of a user defined interface element based on traction-separation laws, are given. The report is meant to assist students starting to gain experience by passing know-how of a previous generation. The examples given at the end may serve as benchmarks.

Contents:

1. Symmetry conditions in FE models

Considering symmetries of structures helps reducing computation time and memory in FE simulations. Particularly, cracks and crack-like defects require a fine discretisation to resolve the high stress and strain gradients resulting in a large number of elements and degrees of freedom.

A 3D structure can have up to three symmetry planes[4], Fig. 1.1.

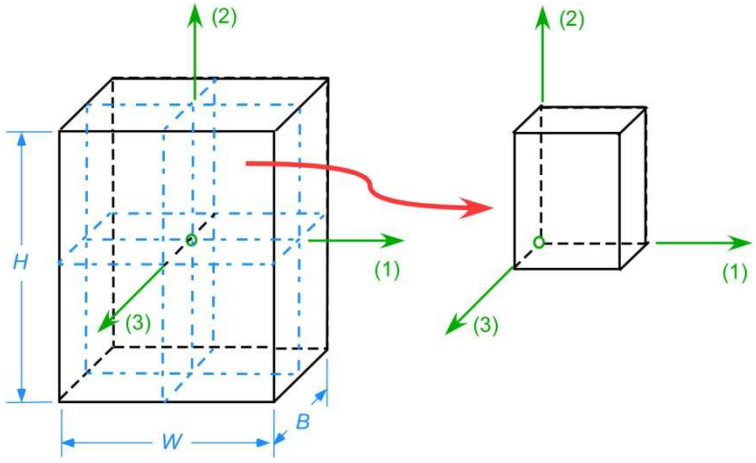

Figure 1.1: Brick with three symmetry planes (left), {3,1}, {2,3}, {1,2}, normal vectors $\mathbf{n}_2 = -\mathbf{e}_2$, $\mathbf{n}_1 = -\mathbf{e}_1$, $\mathbf{n}_3 = -\mathbf{e}_3$, and (1/8) model (right).

Accounting for these symmetries in the FE model will reduce the number of elements up to one eighth and nearly likewise the number of degrees of freedom. The *symmetry* is implemented by inhibiting the displacements, u_i, perpendicular to the symmetry plane of all element nodes in the respective plane by *boundary conditions*, i.e.

$$\begin{aligned} \{2,3\}: &\quad u_1(0,x_2,x_3)=0 \\ \{3,1\}: &\quad u_2(x_1,0,x_3)=0 \\ \{1,2\}: &\quad u_3(x_1,x_2,0)=0 \end{aligned} \tag{1}$$

Applied symmetry conditions affect calculated elongations, namely

$$\begin{aligned} \Delta W &= 2\bar{u}_1(W/2) \\ \Delta H &= 2\bar{u}_2(H/2) \\ \Delta B &= 2\bar{u}_3(B/2) \end{aligned} \tag{2}$$

and hence the volume change,

$$\Delta V = \Delta W \Delta H \Delta B = 8\bar{u}_1(W/2)\bar{u}_2(H/2)\bar{u}_3(B/2) \tag{3}$$

as well as all quantities related to a volume, like deformation energy,

$$U(V) = 8U(V/8) \quad , \tag{4}$$

or to an area, like forces. An external force, F_{model}, applied in $\mathbf{e}_2$ direction at the upper surface of the 1/8 brick model in Fig. 1.1 corresponds to a total force, F_{total}, acting on the structure,

[4] Symmetry must also hold for the loading configuration, of course.

$$F_{\text{total}} = 4F_{\text{model}} = 4\sum_{n} RF_2^{(n)} \tag{5}$$

where Σ_n is the sum over all nodes in the {3,1}-plane and $RF_2^{(n)}$ are the respective reaction forces.

Symmetry conditions do not affect stresses (force per area) according to NEWTON's 3rd principle or CAUCHY`s section principle.

Fig. 1.2 shows two fracture specimens under mode I loading, namely a compact specimen (a) and a centre-cracked panel (b). The C(T) has one symmetry with respect to the horizontal (1) axis and can be modelled as a half model in 2D and a quarter model in 3D (additional symmetry with respect to the {1,2} plane in thickness direction). The M(T) has a twofold symmetry with respect to the horizontal (1) and the vertical (2) axis. It can be modelled as a quarter model in 2D and an eighth model in 3D.

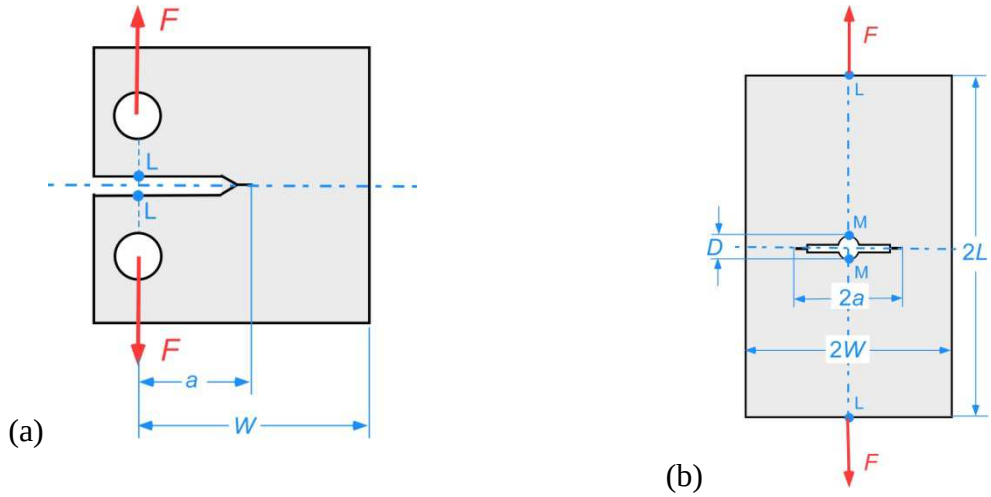

Figure 1.2: Fracture mechanics specimens; (a) compact specimen C(T), (b) centre-cracked panel M(T).

Models of structures containing a crack in a symmetry line (or plane) must allow for opening of the crack faces, and the boundary conditions of eq. (1) are hence restricted to the ligament nodes, i.e.

$$u_2\left(x_1, x_2\right) = 0, \quad x_1 \geq a, \quad x_2 = 0 \tag{6}$$

Typical 2D FE meshes in the vicinity of the crack tip in fracture mechanics specimens under mode I are displayed in Fig. 1.3.

As loading and geometry are symmetric, just the upper half is modelled and normal displacements are constrained in the ligament. Collapsed elements centred to the crack tip are commonly applied for the analysis of stationary cracks (a) and an equidistant element arrangement for the analysis of extending cracks (b), respectively. The boundary conditions are given by eq. (6) with the exception that some node release technique or cohesive elements (see below) have to be applied for the analysis of crack extension, i.e. in the range of $a_0 \leq x_1 \leq a_0 + \Delta a_{\max}$ and boundary conditions $u_2|_{x_2=0} = 0$ for $x_1 \geq a_0 + \Delta a_{\max}$.

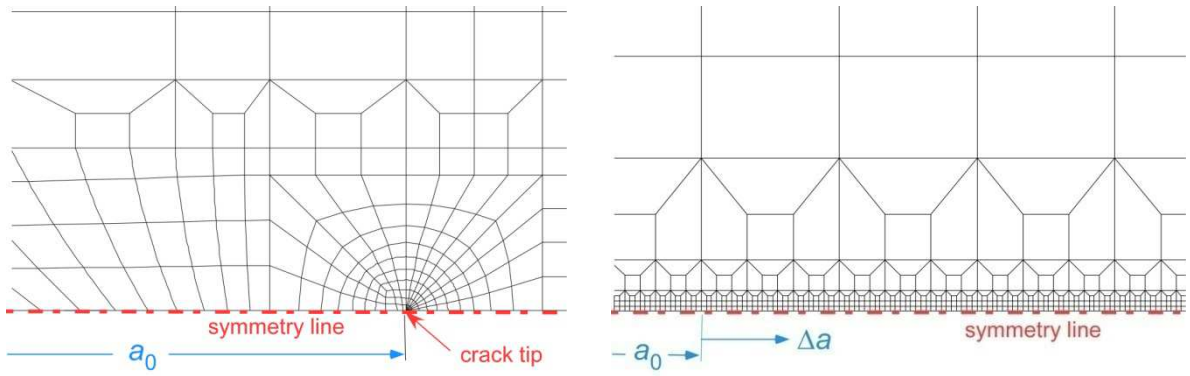

(a) (b)

Figure 1.3: Typical FE meshes at the crack tip and in the ligament: (a) Collapsed elements centred to the crack tip for a stationary crack, (b) equidistant arrangement of elements for simulations of crack extension.

The symmetry conditions affect displacement values like load-point or load-line displacement, V_{LL}, measured between points L in Fig.1.2, crack mouth opening displacement, CMOD, measured between points D in Fig 1.2 (b), crack tip opening displacement (CTOD), δ, and the crack-tip opening angle (CTOA), see Fig. 1.4, which have to be doubled as in eq. (2).

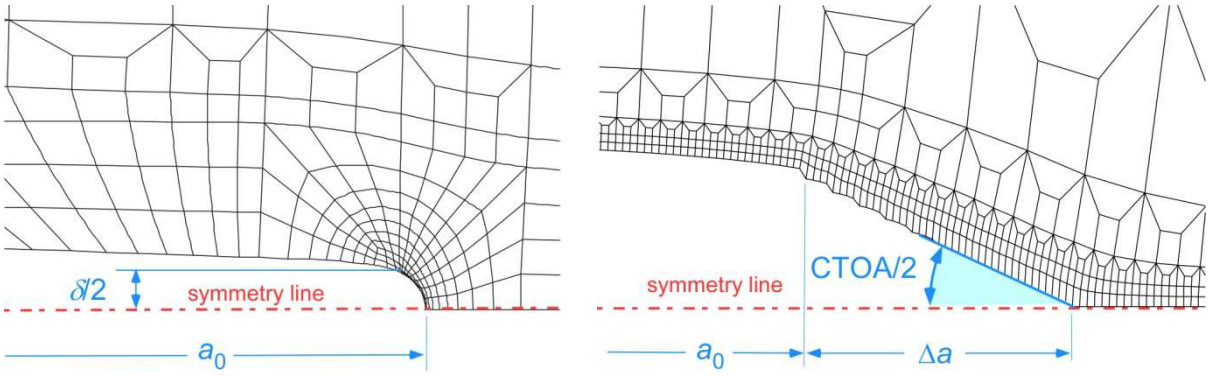

(a) (b)

Figure 1.4: Deformed FE meshes at the crack tip showing (a) blunting of a stationary crack and (b) crack opening due to crack extension.

Also the J-integral value is affected by the symmetry with respect to the x_1-axis, Fig. 1.5.

$$J = \oint_{\Gamma} \left(\bar{w} dx_2 - \sigma_{ij} n_j u_{i,1} ds \right) \qquad (7)$$

$$\bar{w} = \int_{\tau=0}^{t} \sigma_{ij} \dot{\varepsilon}_{ij} d\tau$$

$$J_{\text{total}} = 2 J_{\text{half}} \qquad (8)$$

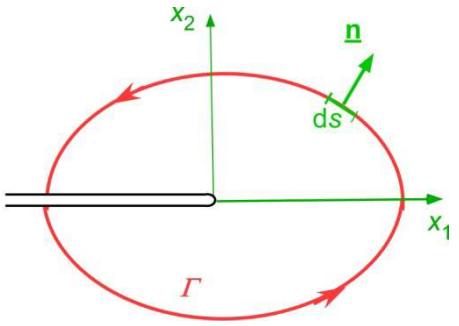

Figure 1.5: Definition of J as contour integral around the crack tip

An additional symmetry with respect to the x_2-axis as for M(T) specimens is irrelevant because it concerns a second crack tip. In 3D models, J is varying along the crack front and calculated in planes x_3 = const for straight cracks or generally perpendicular to the crack front for curved cracks.

2. Cohesive elements - general

The cohesive model is a phenomenological model of material separation based on ideas of BARENBLATT and DUGDALE. ABAQUS [1] offers a library of cohesive elements to model the behaviour of adhesive joints, interfaces in composites, and other situations where the integrity and strength of interfaces may be of interest. It can likewise be used for the simulation of crack extension in homogeneous materials where there is no specific interface but just a "process zone", where material degradation (nucleation, growth and coalescence of micro-cracks, micro-voids or micro-cavities) and final separation occur.

Cohesive elements can be used for all problems where cracks develop and extend. However, the model does not need any initial, pre-existing crack. The locations (among all areas modelled with cohesive elements) where cracks initiate, as well as the evolution characteristics of such cracks, are determined as part of the solution. The cracks are restricted to propagate along the pre-defined layer of cohesive elements, however, and will not deflect into the surrounding material.

The nature of the mechanical constitutive response may broadly be classified [1] to be based on

- a continuum (C) description of the material,
- a traction-separation (TS) description of the interface.

2.1 Continuum-based modelling

A continuum-based modelling of an adhesive connecting two bodies is appropriate when the glue has a finite thickness. The macroscopic properties, such as stiffness and strength, of the adhesive material can be measured experimentally, if the connected bodies are linear elastic, and used directly for modelling purposes [2]. The adhesive material is generally more compliant than the surrounding material. The cohesive elements model the initial deformation, the initiation and the propagation of damage leading to eventual failure in the material. For further information see the ABAQUS manual [1], section 32.5.5.

As the respective elements are continuum elements, symmetry conditions can be applied as described above. The first layer of elements in the crack ligament as shown in Fig 1.3 (b), may represent an adhesive of half thickness modelled by C-based elements.

2.2 Traction-separation-based modelling

The intermediate "glue material" of bonded interfaces can be very thin and for all practical purposes may be considered to be of zero thickness. In this case, its deformation behaviour is not relevant, and GRIFFITH's concept of fracture mechanics applies [3], considering the amount of energy required to create new surfaces. The TS-based model has hence also found wide application to fracture mechanics problems, where the "interface" is fictitious and does

not represent any “glue material” but a process zone of zero thickness, where material degradation and separation is localised, see e.g. overview in [4].

The behaviour of the material is actually split in two parts, the damage-free continuum with an arbitrary constitutive law, and the cohesive interfaces between the continuum elements, which capture the damage of the material. The interface elements open during loading and finally lose their stiffness if a critical separation, δ_c, is reached, such that the continuum elements are disconnected. The *separation* of the cohesive interfaces is calculated from the displacement jump, i.e. the difference of the displacements of the adjacent continuum elements,

$$\delta_n = [u_2] = u_2^+ - u_2^- \tag{9}$$

As the focus of the present report is on symmetry conditions, the considerations are restricted to mode I problems and normal separation, δ_n, only.

The normal stresses or *tractions*, σ_n, follow a traction-separation law (TSL), $\sigma_n(\delta_n)$, also denoted as cohesive law or decohesion law, which depends on two parameters,

- a maximum stress or *cohesive strength*, σ_c, and
- a *critical separation*, δ_c.

Various authors have suggested a number of cohesive laws for different applications and mechanisms of fracture, see Fig. 2.1 and an overview in [4].

The area under the $\sigma_n(\delta_n)$ curve represents the energy necessary to create new surfaces, i.e. the GRIFFITH or *separation energy*

$$\Gamma_c = \int_0^{\delta_c} \sigma_n(\delta_n)\, d\delta_n \tag{10}$$

Beside the TS-based cohesive element provided by ABAQUS [1][5], section 32.5.6, a user defined interface element of zero thickness has been developed by SCHEIDER [5] incorporating traction-separation laws of NEEDLEMAN [6],

$$\sigma_n(\delta_n) = \sigma_c \frac{16\,e^2}{9}\frac{\delta_n}{\delta_c}\exp\left(-\frac{16\,e}{9}\frac{\delta_n}{\delta_c}\right), \quad e = \exp(1); \tag{11a}$$

TVERGAARD & HUTCHINSON [7]

$$\sigma_n(\delta_n) = \sigma_c \begin{cases} \left(\dfrac{\delta_n}{\delta_1}\right) & \delta_n \le \delta_1 \\ 1 & \delta_1 \le \delta_n \le \delta_2 \\ \left(\dfrac{\delta_c - \delta_n}{\delta_c - \delta_2}\right) & \delta_2 \le \delta_n \le \delta_c \end{cases}, \tag{11b}$$

and SCHEIDER [8],

[5] In addition to the TS based cohesive element, cohesive behaviour can also be defined and modelled as a surface interaction property (`*SURFACE INTERACTION`) in ABAQUS.

$$\sigma_n(\delta_n) = \sigma_c \begin{cases} 2\left(\frac{\delta_n}{\delta_1}\right) - \left(\frac{\delta_n}{\delta_1}\right)^2 & \delta_n \le \delta_1 \\ 1 & \delta_1 \le \delta_n \le \delta_2 \\ 1 + 2\left(\frac{\delta_n - \delta_2}{\delta_n - \delta_2}\right)^3 - 3\left(\frac{\delta_n - \delta_2}{\delta_n - \delta_2}\right)^2 & \delta_2 \le \delta_n \le \delta_c \end{cases}, \tag{11c}$$

see Fig. 2.1, and some special features like mixed-mode loading and dependence of cohesive parameters on external state variables. The following considerations will mostly refer to this user element.

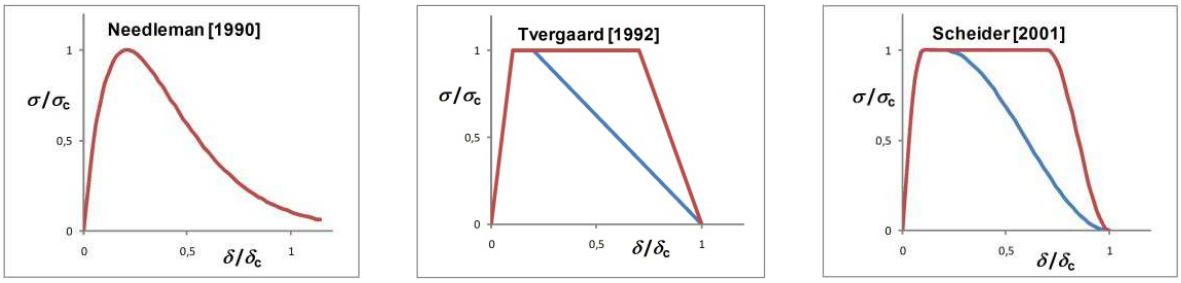

(a) (b) (c)

Figure 2.1: Traction-separation laws, $\sigma(\delta)$, of (a) NEEDLEMAN [6], (b) TVERGAARD & HUTCHINSON [7] and (c) SCHEIDER [8].

The TSLs of TVERGAARD & HUTCHINSON and SCHEIDER contain two additional shape parameters, δ_1 and δ_2, defining the initial slope of the curve and the starting point of softening, respectively. In order to endow the cohesive element with a high initial stiffness, see ELICES et al. [9], δ_1 should be chosen as small as (numerically) possible. The initial stiffness of the cohesive element,

$$K_{coh} = \left(\frac{d\sigma}{d\delta}\right)_{\delta=0} = \begin{cases} \frac{\sigma_c}{\delta_2} & \text{TVERGAARD} \\ \frac{2\sigma_c}{\delta_2} & \text{SCHEIDER} \end{cases}, \tag{12a}$$

should at least be greater than the elastic stiffness of the adjacent continuum element,

$$K_{coh} > \frac{E}{h}, \tag{12b}$$

where h is the height of the continuum element, which yields a condition for δ_1. The second shape parameter, δ_2, will depend on the fracture process and hence be material dependent.

In NEEDLEMAN's model [6], Fig. 2.1 (a), the initial stiffness is uniquely determined by σ_c and δ_c and cannot be defined separately,

$$K_{coh} = \left(\frac{d\sigma}{d\delta}\right)_{\delta=0} = \frac{16e^2}{9}\frac{\sigma_c}{\delta_c} \approx 13\frac{\sigma_c}{\delta_c} \quad \text{NEEDLEMAN}, \tag{12c}$$

3. Embedding of cohesive elements in FE models

3.1. 2D and 3D models

TS-type cohesive elements have been developed in [5] for 2D and 3D models as well as for shell structures. They have one dimension less than the adjacent continuum elements, but have an upper and a lower surface, nevertheless, denoted with (+) and (-) in the following, which are attached to continuum elements and open during loading. Even though a cohesive element has no volume in the unloaded and undamaged state, it will be called 2D or 3D cohesive element in the following, if the neighbouring structure consists of 2D or 3D continuum elements, respectively.

2D 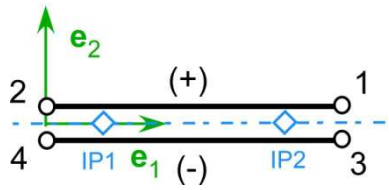 (a)	3D 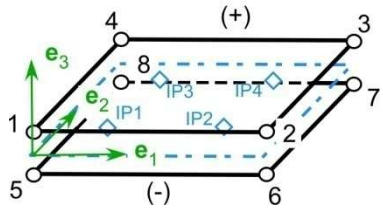 (b)
*USER ELEMENT, TYPE=U2, NODES=4	*USER ELEMENT, TYPE=U5, NODES=8

Figure 3.1: 2D and 3D TS-type cohesive elements [5]

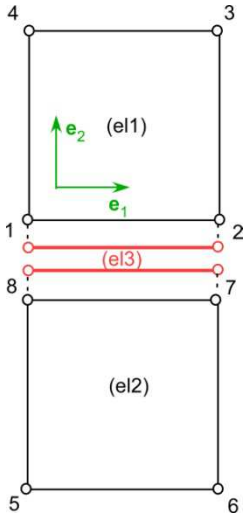 (a)	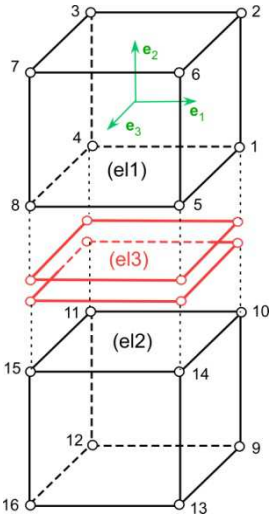 (b)
*ELEMENT,TYPE=CPE4 1, 1, 2, 3, 4, 2, 5, 6, 7, 8, *ELEMENT, TYPE=U2 3, 2, 1, 7, 8,	*ELEMENT,TYPE=C3D8 1, 1, 2, 3, 4, 5, 6, 7, 8, 2, 9, 10, 11, 12, 13, 14, 15, 16, *ELEMENT, TYPE=U5 3, 8, 5, 1, 4, 15, 14, 10, 11,

Figure 3.2: Connecting cohesive and continuum elements

2D cohesive elements have four nodes with a linear displacement formulation and two integration points, see Fig. 3.1 (a). Elements are implemented for plane strain, plane stress and for axisymmetric problems. 3D elements can have a linear displacement formulation using

eight nodes, see Fig. 3.1 (b), or quadratic shape functions with 16 or 18 nodes. Stresses are calculated at the integration points according to the TSL.

Introducing a cohesive element at the boundary of two adjacent continuum elements means connecting the nodes at its upper and lower surface with the respective nodes of the continuum elements. This is straightforward in a 2D structure, see Fig. 3.2 (a). In a 3D structure one has to observe differing local coordinate systems and consider a correct mathematically positive, i.e. counter-clockwise, numbering of nodes at the upper surface of the cohesive element, see Fig. 3.2 (b). Note that the opening direction of the cohesive element is $\mathbf{e}_3$ in the local coordinate system, see Fig. 3.1 (b).

The local coordinate system of the cohesive element is fixed to the mid-plane and, depending on the specification by the user, will move according to the deformation of the continuum elements.

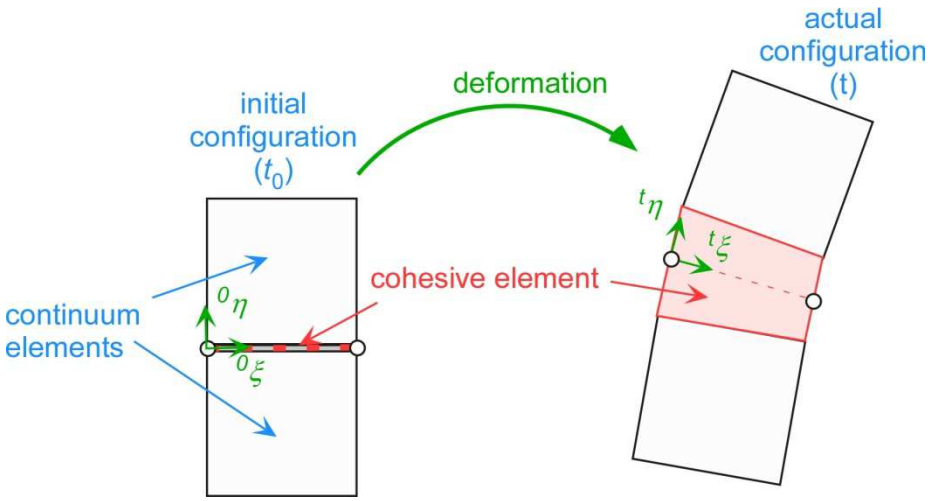

Figure 3.3: Definition and motion with time of the local coordinate system ofa cohesive element, $\xi \leftrightarrow \mathbf{e}_1$, $\eta \leftrightarrow \mathbf{e}_2$ in Fig. 3.1 (a).

The respective parameter `coord_flag` can have the values "0" and "1", where `coord_flag=0` keeps the local coordinate system fixed at the reference plane, whereas for `coord_flag=1` the actual configuration is used, see Fig. 3.3.

In general, mode II shear deformation will occur if the cohesive element is subject to any global rotation. For pure mode I separation, geometry and loading have to be symmetric to the separation plane and hence symmetry conditions can be exploited.

3.2. Cohesive elements at symmetry planes

The following figures display 2D models, only, but can easily be generalised to 3D situations.

If a cohesive element is placed at a line (plane) of symmetry, it will undergo an unsymmetric deformation if, following eq. (1), simply the displacements $u_2^{(-)}$ of the lower surface are constrained, see Fig 10 (a). The midplane will rotate and the displacements $u_1^{(-)}$ and $u_3^{(-)}$will be different from $u_1^{(+)}$ and $u_3^{(+)}$ resulting in respective displacement jumps and shear separation, $\delta_{t1} = [u_1] = u_1^+ - u_1^-$, $\delta_{t3} = [u_3] = u_3^+ - u_3^-$. This can be prevented by choosing `coord_flag=0`, which keeps the local coordinate system fixed at the reference plane, and additional constraint equations $u_1^{(-)} = u_1^{(+)}$ and $u_3^{(-)} = u_3^{(+)}$, see Fig. 3.4(b). According to

eq. (2), the critical displacement has to be taken as $\delta_c/2$, and the resulting separation energy will be $\Gamma_c/2$.

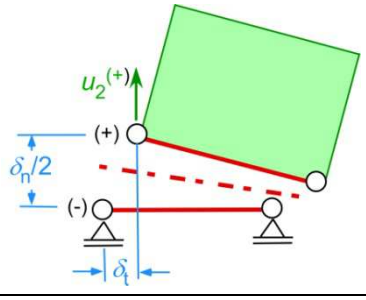	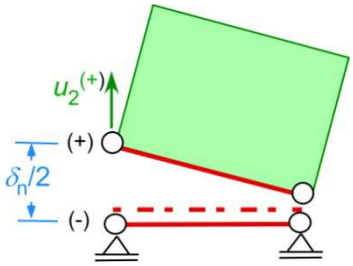	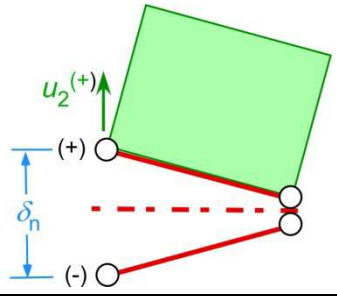
$u_2^{(-)} = 0$ `coord_flag` = 1	$u_2^{(-)} = 0$ $u_1^{(-)} = u_1^{(+)}$ `coord_flag`= 0	$u_2^{(-)} = -u_2^{(+)}$ $u_1^{(-)} = u_1^{(+)}$ `coord_flag`= 0 or 1
no symmetry, mixed mode!	`delta_N`=$\delta_c/2$, `traction_N`=σ_c	`delta_N`=δ_c, `traction_N`=$\sigma_c/2$
(a)	(b)	(c)

Figure 3.4: Cohesive elements at symmetry lines: Boundary conditions, constraint equations and input variables.

A second possibility of realising symmetry is to establish constraint conditions $u_2^{(-)} = -u_2^{(+)}$, which guarantee a symmetric opening of the cohesive element, $\delta_n = u_2^{(+)} - u_2^{(-)} = 2u_2^{(+)}$, and thus keeping the entire δ_c, see Fig. 3.4 (c). There is some unexpected consequence of applying constraint equations in ABAQUS [9], however. They induce extra nodal forces[6], which reduce the stresses in the respective element to one half, so that the cohesive strength has to be taken as $\sigma_c/2$. This will be discussed in more detail in the following paragraph.

Since ABAQUS has no access to the stress and strain state in User Elements, only the continuum elements contribute to the calculation of *J*. As the cohesive elements have no volume (or a negligibly small one if $\delta_1 \le \delta_n \le \delta_c$), however, the tractions σ_n will not affect *J* for any contour or domain in some finite distance to the crack tip. Just for a contour directly at the crack tip,

$$J_{tip} = \int \sigma_n d\delta_n \ . \tag{13}$$

3.3. Constraint forces and global equilibrium

"Linear constraint equations introduce constraint forces at all degrees of freedom appearing in the equations. These forces are considered external, but they are not included in reaction force output. Therefore, the totals provided at the end of the reaction force output tables may reflect an incomplete measure of global equilibrium." [10]

[6] "Linear constraint equations introduce constraint forces at all degrees of freedom appearing in the equations. These forces are considered external, but they are not included in reaction force output. Therefore, the totals provided at the end of the reaction force output tables may reflect an incomplete measure of global equilibrium." [10]

The ABAQUS Manual provides the following example of a spring-supported beam subjected to a concentrated load, see Fig. 3.5 (a). The static reaction forces are $R_C = F/3$ and $R_D = 2F/3$. In Fig. 3.5 (b), the same structure is subjected to the additional linear constraint equation $u_y^A - u_y^B = 0$, which constrains the beam to remain horizontal. This introduces constraint forces $F_A = -F_B = F/6$ and the new reaction forces are $R_C = R_D = F/2$. These reaction forces produce a global force balance in the *y*-direction, but since the constraint forces are not included in the reaction force output, the global moment balance about point A cannot be verified.

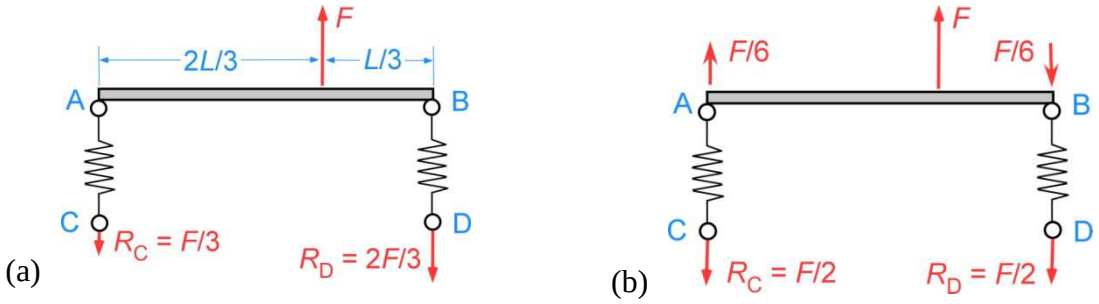

Figure 3.5: Spring-supported beam subjected to a concentrated load [10], effect of constraint equations.

Whereas this example appears rather plausible, since additional forces are required to keep the beam horizontal, the following one shows a rather unexpected result.

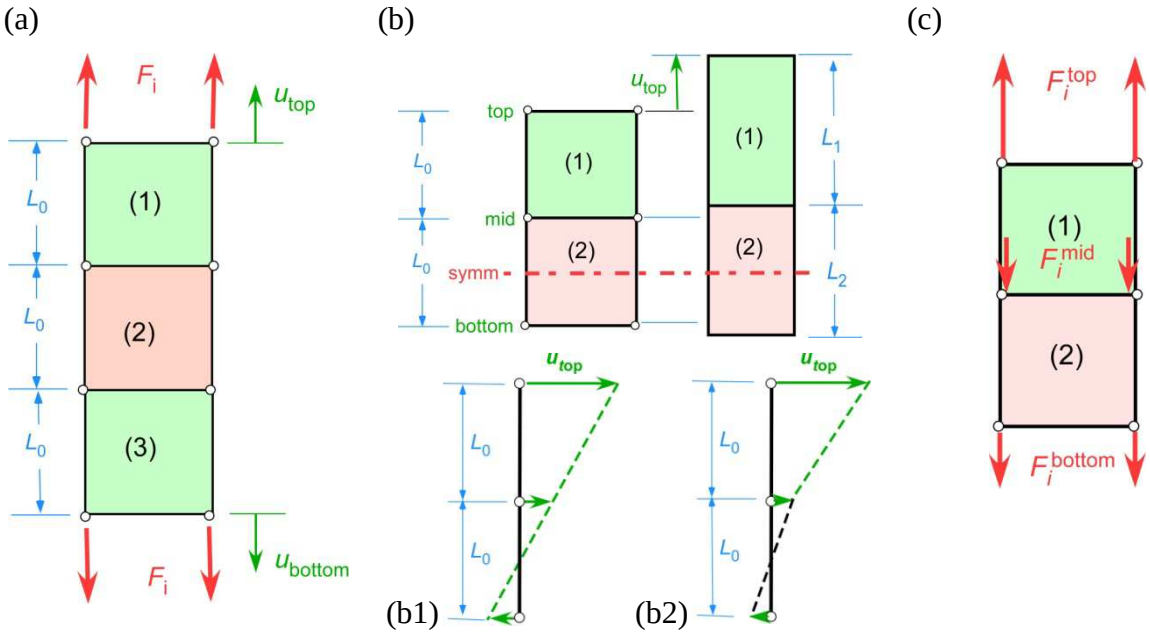

Figure 3.6: Model of a tensile bar, effects of constraint equations.

Consider a simple model of a tensile bar with quadratic cross section, A_0, as an assembly of three elastic continuum elements of length L_0 subjected to a total uniform elongation of ΔL which is symmetrically applied as displacements,

$$u_{\text{upper}} = -u_{\text{lower}} = \frac{\Delta L}{2} \tag{14a}$$

at the upper and the lower surface, respectively, see Fig. 3.6 (a). Stresses are uniform and identical for all elements,

$$\sigma^{(1)} = \sigma^{(2)} = \sigma^{(3)} = \sigma = E\varepsilon = \frac{1}{3} EA_0 \frac{\Delta L}{L_0} \ , \tag{15a}$$

and the reactions forces at the four nodes at the top and the bottom surface are

$$F_i^{\text{top}} = F_i^{\text{bottom}} = \frac{1}{4}\sigma A_0 = \frac{1}{12} EA_0 \frac{\Delta L}{L_0} \ . \tag{16a}$$

Now, one might expect that the same result can be obtained by considering just two elements and inserting a symmetry plane in the centre of element (2), introducing a constraint equation,

$$u_{\text{bottom}} = -u_{\text{mid}} \ , \tag{14b}$$

and applying $u_{\text{top}} = \Delta L/2$ as before, see Fig. 3.6 (b). The corresponding kinematics supposed to be realised is shown in Fig. 3.6 (b1), and the results for the stresses to be the same as above.

However, the FE analysis yields stresses in the two elements that are not equal anymore,

$$\sigma^{(1)} = 2\sigma^{(2)} = \frac{2}{5} EA_0 \frac{\Delta L}{L_0} \ , \tag{15b}$$

and nodal forces at the top and the bottom are different, apparently violating overall equilibrium,

$$F_i^{\text{top}} = 2F_i^{\text{bottom}} = \frac{1}{4}\sigma^{(1)} A_0 = \frac{1}{10} EA_0 \frac{\Delta L}{L_0} \ . \tag{16b}$$

The kinematics of the structure is not the expected one of Fig. 3.6 (b1) but that of (b2) with

$$u_{\text{mid}} = \frac{1}{5} u_{\text{top}} \ , \quad \Delta L_1 = 2\Delta L_2 = \frac{4}{5} u_{\text{top}} \tag{14c}$$

and constraint forces are applied as external forces,

$$F_i^{\text{mid}} = \frac{1}{2} F_i^{\text{top}} = F_i^{\text{bottom}} \ , \tag{16c}$$

see Fig. 3.6 (c), which "are not included in reaction force output" [10].

This finally explains why the cohesive tractions in the symmetry model according to Fig. 3.4 (c) are only half of the "real" ones (apparently violating CAUCHY's section principle), and hence $\sigma_c/2$ has to be provided as input.

4. Simulation examples

4.1. Ductile crack extension in a centre-cracked panel (plane stress and 3D analysis)

Geometry:	width	$2W$ = 300 mm
	initial crack length	$2a$ = 60 mm
	thickness	B = 2.9 mm
	length	$2L = 1.5 \cdot 2\,W$ = 450 mm
Material:	Al 5083	
	YOUNG's modulus	E = 70300 MPa
	Poisson's ratio	ν = 0.3
	0.2% proof stress	$R_{p0.2}$ = 242 MPa

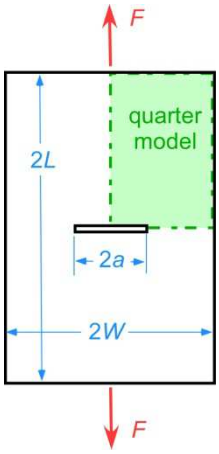

Respective tests have been performed at GKSS Research Centre, Geesthacht, Germany, see SCHEIDER et al. [11].

The true stress-strain curve, $\sigma(\varepsilon_p)$, required as input for ABAQUS has been determined from tensile test data of a flat bar with rectangular cross section, width W_0 = 8.01 mm, thickness B_0 = 2.9 mm, measuring length L_0 = 30 mm. As the test data end at a plastic strain value of ε_p = 0.12 and much higher values are to be expected at the crack tip of the M(T) specimen, the stress strain curve has been fitted and extrapolated by a power law, see Fig. 4.1.1. Note that $R_{p0.2}$ = 242 MPa whereas a yield limit of $R_0 = \sigma(\varepsilon_p{=}0)$ = 200 MPa is used as input for ABAQUS.

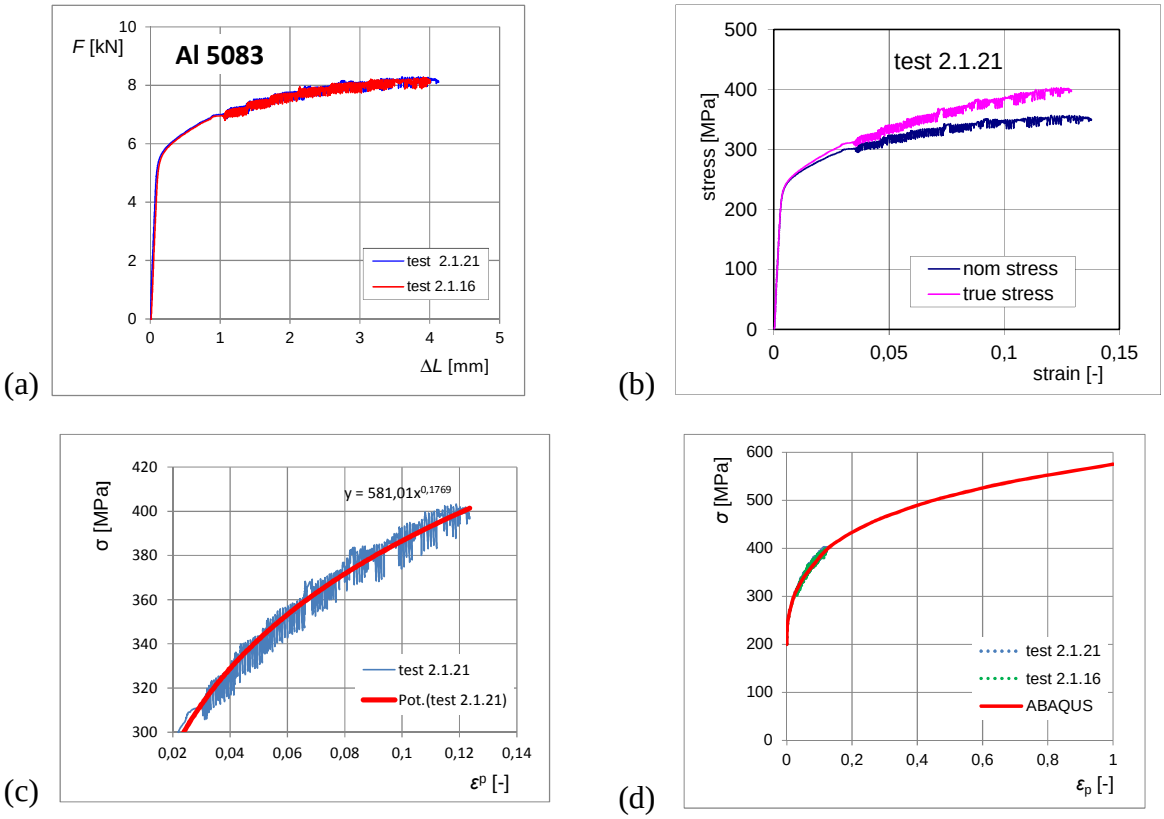

Figure 4.1.1: Deriving a uniaxial stress-strain curve as input for ABAQUS from test data: (a) Force vs. elongation of tensile test, (b) nominal and true stresses vs. linear and logarithmic strain, respectively, (c) fitting of $\sigma(\varepsilon_p)$ by a power law, (d) ABAQUS input.

The User-Element and the cohesive law of SCHEIDER [5, 8] are employed, see Fig. 4.1.2.

cohesive strength	$\sigma_c = 2.31\ R_{p0.2} = 560$ MPa (2D),
	$\sigma_c = 2.64\ R_{p0.2} = 640$ MPa (3D)
critical separation	$\delta_c = 0.024$mm
separation energy	$\Gamma_c = 9.86$ kJ/m^2 (2D), 11.26 kJ/m^2 (3D)
shape parameters	$\delta_1 = 0.05\ \delta_c$, $\delta_2 = 0.5\ \delta_c$

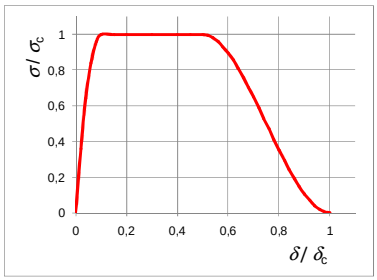

Figure 4.1.2: Cohesive law

Whereas the uniaxial stress-strain curve can be directly deduced from tensile test data, the identification of cohesive parameters is an inverse process of fitting simulations to the data of fracture tests like load vs. displacement records or R-curves [12]. The cohesive parameters applied in 2D have been determined by SCHEIDER et al. [11]. The shape parameters may be taken more or less identical for all ductile metals. Whereas δ_1 should be as small as (numerically) possible in order to endow the cohesive element with a high initial stiffness, $\delta_2 = 0.5\ \delta_c$ proved successful for aluminium alloys as well as for steels.

A quarter model exploiting the twofold symmetry of the M(T) specimen is used in 2D and 1/8 model (threefold symmetry) in 3D. Respective boundary conditions are applied along the *x*- and *y*-axis in 2D and in the {*zx*}-, {*yz*}- and {*xy*}-plane in 3D as described by eqs. (1), (6). The 2D mesh design is shown in Fig 4.1.3. Cohesive elements are placed along the symmetry line as in Fig. 1.3 (a). Both models (b) and (c) of Fig. 3.4 have been used for establishing symmetry conditions in 2D.

For the2D plane stress analysis, the option

```
*THICKNESS DEPENDENCE
```

has to be used [5]. This keyword assigns the plane cohesive elements to be thickness dependent. Since the thickness is determined from the adjacent continuum elements, the keyword

```
*ELEMENT MAP
```

is required to define the connection between the cohesive elements and the respective adjacent continuum elements.

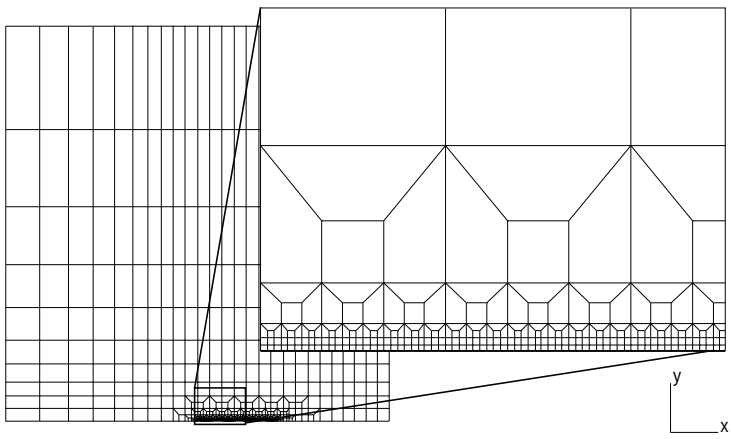

Figure 4.1.3: FE mesh of the M(T) showing mesh refinement at the crack ligament, element size 0.125 mm.

The simulation is run displacement controlled, i.e. a uniform displacement, u_2, is applied at the upper surface and the total force, F, is calculated from the respective reaction forces, RF_2,

$$F = \begin{cases} 2\sum_n RF_2^{(n)} & 2D \\ 4\sum_n RF_2^{(n)} & 3D \end{cases} . \qquad (17)$$

Fig. 4.1.4 shows comparisons between test and 2D simulation results in terms of force vs. load-point displacement, V_{LL}, and CTOD, δ_5, [13] vs. crack extension. Test results are well matched by the simulations. Both realisations of symmetry according to Fig. 3.4 (b), based on boundary conditions with `delta_N` = $\delta_c/2$, and Fig. 3.4 (c), based on constraint equations with `traction_N` = $\sigma_c/2$, yield practically identical results, demonstrating that they are equivalent.

The force vs. load-point displacement curves differ for the two tests, whereas no significant difference exists for the respective R-curves. The former is due to the buckling behaviour of the two specimens: M(T) 2.1.8 was equipped with an anti-buckling device whereas M(T) 1.1.3 was not, which affects the global but not the local behaviour in terms of $\delta_5(\Delta a)$. The onset of mechanical instability at maximum force is a process, which is sensitive to imperfections in real testing as well as in the simulations (see also the results of tensile tests in Fig. 4.2.1 (a), below). Parameter identification should hence preferably be based on test records of local quantities, particularly R-curves of crack extension.

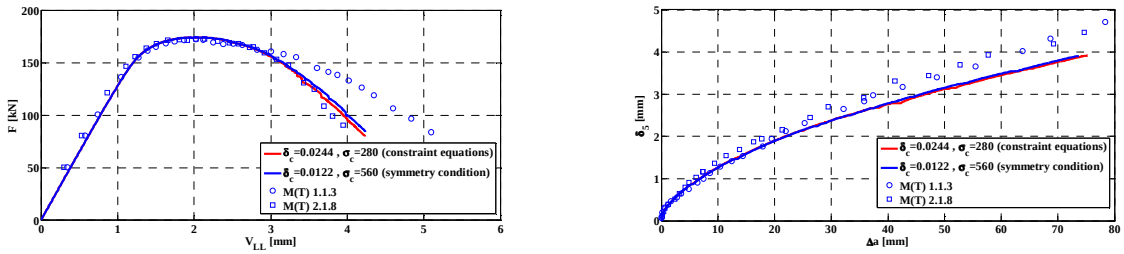

(a) (b)

Figure 4.1.4: Comparison between results of tests and simulations (2D plane stress): (a) load, F, vs. load-point displacement, V_{LL}; (b) R-curve: crack tip opening displacement (CTOD), δ_5, vs. crack extension, Δa; blue curve: symmetry conditions according to Fig. 3.4 (b), red curve: Fig. 3.4 (c).

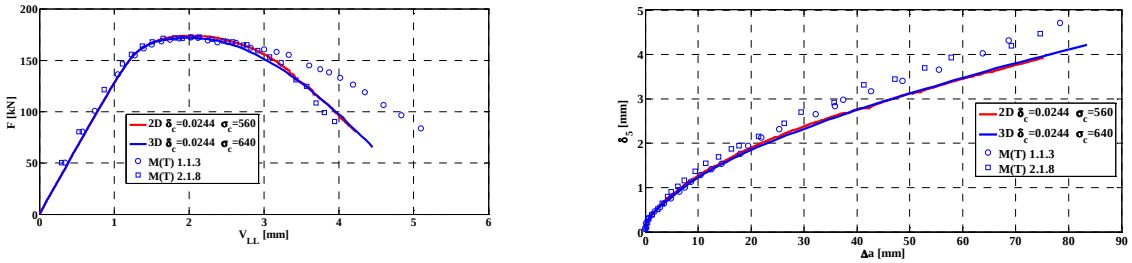

(a) (b)

Figure 4.1.5: Comparison between results of tests and simulations (2D plane stress and 3D): (a) load, F, vs. load-point displacement, V_{LL}; (b) R-curve: crack tip opening displacement (CTOD), δ_5, vs. crack extension, Δa; 2D: red curve, 3D: blue curve.

The cohesive parameters obtained for a 2D plane-stress model will in general differ from the parameters suited for a 3D model [14]. Even if the *global* response of the structure is well met by the assumption of a plane stress state, the *local* stress state varies over the thickness and triaxiality is higher in the centre than at the surface. In the present example, a cohesive strength of $\sigma_c = 2.64\, R_{p0.2} = 640$ MPa yielded a perfect coincidence between the 2D and the 3D (1/8) model, Fig. 4.1.5.

Fig. 4.1.6 shows the "tunnelling" or "thumb-nail" shape of the crack front. Due to symmetry with respect to the {*x*,*y*} plane, the depicted zoom of the FE mesh represents one half of the crack plane. The colours indicate maximum principle stress.

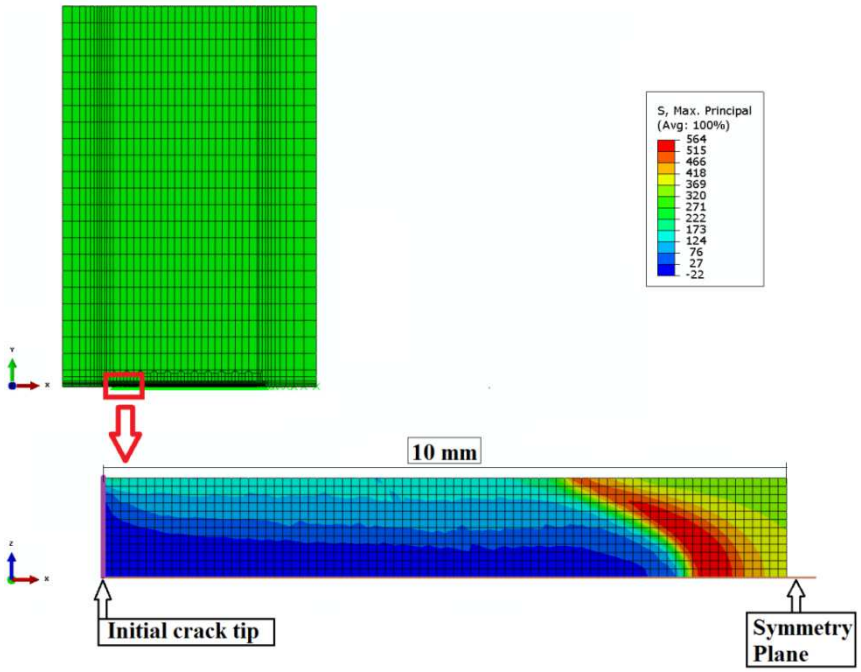

Figure 4.1.6: 3D FE model of the M(T) specimen with zoomed view of the {*x*,*z*} plane.

4.2. Ductile crack extension in a compact specimen (plane strain analysis)

Geometry:	width	W = 50 mm
	initial crack length	a = 33.2 mm
	net thickness	B_n = 20 mm
	(20% side grooved)	
Material:	26NiCrMoV115	
	YOUNG's modulus	E = 204400 MPa
	Poisson's ratio	ν = 0.3
	0.2% proof stress	$R_{p0.2}$ = 709 MPa

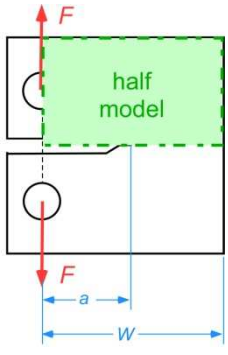

The true stress-strain curve, $\sigma(\varepsilon_p)$,has been determined from data of a standard tensile test with a round bar of diameter $d_0 = 6$ mm, measuring length $L_0 = 30$ mm. The stress-strain curve beyond uniform elongation has been extrapolated based on a power law fit, see Fig. 4.2.1. A yield limit of $R_0 = \sigma(\varepsilon_p{=}0) = 650$ MPa is used as input for ABAQUS.

The User-Element and the cohesive law of SCHEIDER [5, 8] as shown in Fig. 4.1.2 are employed again. The cohesive parameters have been varied in order to fit the experimental

$F(V_{LL})$ and $V_{LL}(\Delta a)$ data[7]. Simulations for three selected parameter sets as shown in the following Table are presented and discussed below.

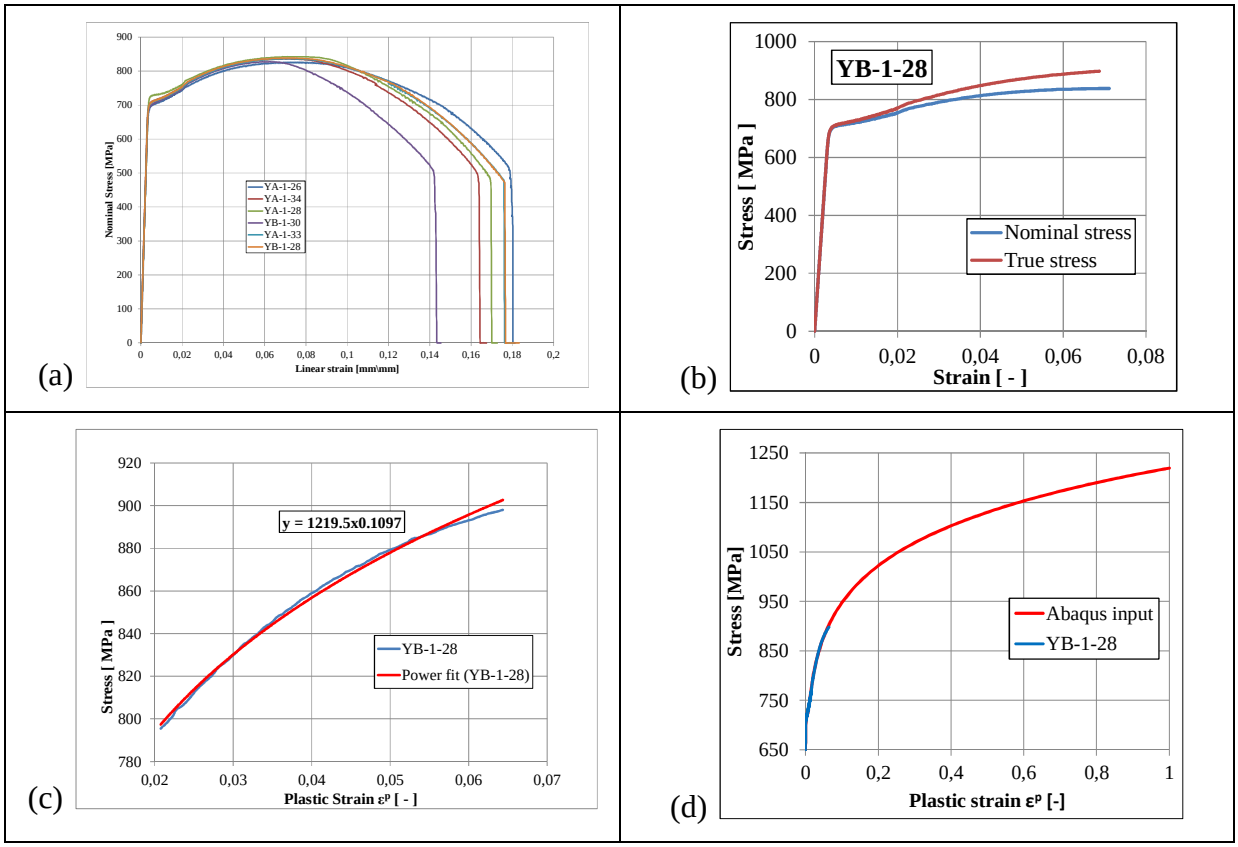

Figure 4.2.1: Deriving a uniaxial stress-strain curve as input for ABAQUS from test data: (a) Nominal stress, F/A_0, vs. linear strain, $\Delta L/L_0$, of tensile tests, (b) nominal and true stresses vs. linear and logarithmic strain, respectively, up to uniform elongation, (c) fitting of $\sigma(\varepsilon_p)$ by a power law, (d) ABAQUS input.

		A	B	C
cohesive strength σ_c	MPa	2127	2836	3049
critical separation δ_c	mm	0.0948	0.00974	0.00974
separation energy Γ_c	kJ/m^2	130	23.3	22.1
shape parameter δ_1/δ_c	-	0.02	0.02	0.02
shape parameter δ_2/δ_c	-	0.3	0.7	0.5

Note that the cohesive strength in the plane-strain simulations, $3 \leq \sigma_c/R_{p0.2} \leq 4.3$, is significantly higher than in the plane-stress case above.

A half model of the C(T) specimen is used, and respective boundary conditions are applied along the *x*-axis. The mesh design is shown in Fig 4.2.2. The simulation is run displacement controlled, i.e. a displacement u_2 is applied to the node in the centre of the load transmission and the respective reaction force represents the applied external force, *F*. In order to avoid

[7] According to ASTM 1820 [15], the data can be easily converted into a J_R curve showing the same qualitative behaviour as the $V_L(\Delta a)$ curve, which has been chosen here as it represents directly measured data.

localisation of plastic deformations in this point, the surrounding domain is assumed as elastic.

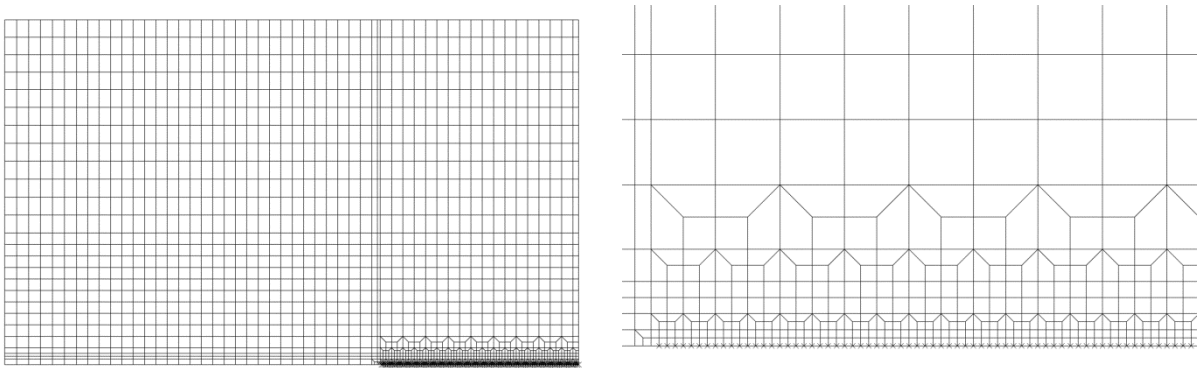

Figure 4.2.2: FE mesh of the C(T) with zoom of the crack ligament, element size 0.125 mm.

An apparently "perfect" coincidence between experimental and numerical data of the $F(V_{LL})$ curve is achieved for parameter set A, see Fig. 4.2.3 (a). The respective *initial resistance to crack extension*, which is dominated by δ_c or Γ_c[8], is significantly overestimated, however, as shown in Fig. 4.2.3 (b). The lesson to be learned is that any coincidence with experimental data of the global load vs. displacement is not a unique indicator that the cohesive parameters have been identified correctly. One has to make sure that crack extension is predicted adequately, e.g. based on a *J* or CTOD R-curve.

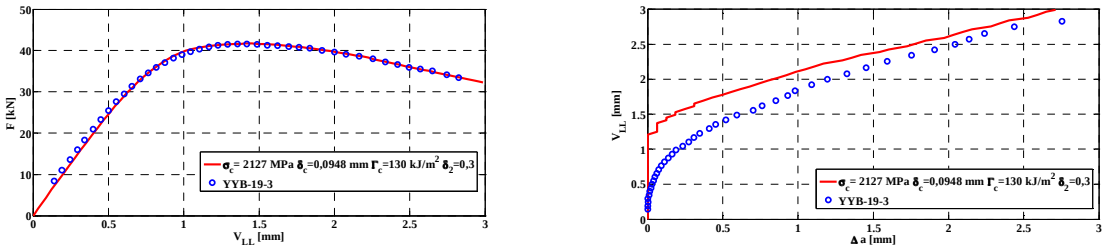

(a) (b)

Figure 4.2.3: Comparison between test results and simulations for parameter set A:
(a) load, *F*, vs. load-line (crack opening) displacement, V_{LL};
(b) load-line displacement, V_{LL}, vs. crack extension, Δa.

Reducing the separation energy, Γ_c, requires increase of the cohesive strength σ_c. Two parameter sets, B and C, with $\sigma_c = 4\ R_{p0.2}$ and $4.3\ R_{p0.2}$, respectively, have been found with approximately the same effect on the macroscopic behaviour, see Figs. 4.2.4 and 4.2.5. Both yield some underestimation of the maximum load by approximately 7%. Apparently, initiation and subsequent crack extension cannot be met simultaneously. Whether this is an effect of the 2D model has to be studied on a 3D model. Applied to a component, the parameter sets B and C are expected to yield conservative predictions of the ultimate strength.

[8] Note that $\Gamma_c \leq J_i$, where J_i denotes the initiation of crack extension, not to be mistaken with J_{IC} according to ASTM 1820 [15].

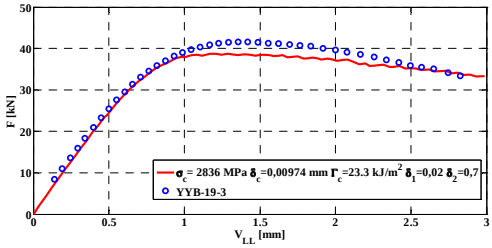

(a)

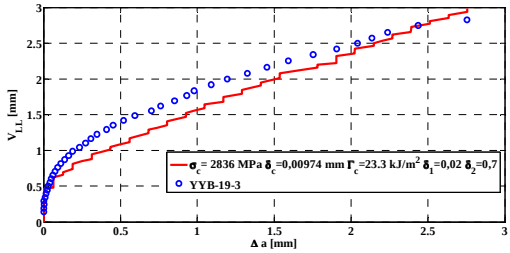

(b)

Figure 4.2.4: Comparison between test results and simulations for parameter set B: (a) load, F, vs. load-line displacement, V_{LL}; (b) load-line displacement, V_{LL}, vs. crack extension, Δa.

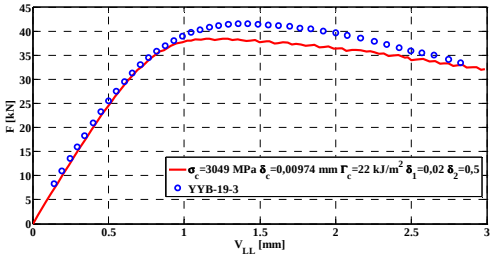

(a)

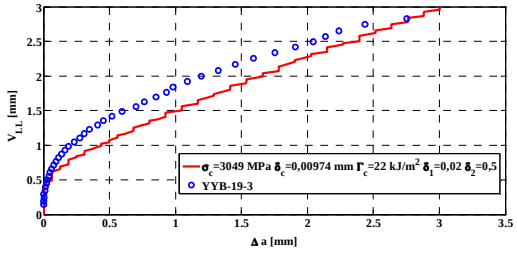

(b)

Figure 4.2.5: Comparison between test results and simulations for parameter set C: (a) load, F, vs. load-line displacement, V_{LL}; (b) load-line displacement, V_{LL}, vs. crack extension, Δa.

Acknowledgement

The present report emerged from intensive work and discussions with PhD students of the Politecnico di Milano during a two months' stay of the first author, who wants to thank

- the students and colleagues of the Dipartimento di Meccanica for their hospitality, commitment and support,
- the department for providing the financial sponsorship, and
- particularly Prof. Stefano Beretta for his invitation and persisting friendship.

The authors also thank Dr. MANFRED SCHÖDEL and Prof. STEFANO FOLETTI for the experimental data of the examples 4.1 and 4.2.

References

[1] ABAQUS Analysis User's Manual (6.11): 32.5 Cohesive elements.

[2] Sørensen, B.F.; Jacobsen, T.K.: Determination of cohesive laws by the *J* integral approach. Eng. Fract. Mech. 70 (2003), 1841-1858.

[3] Brocks, W.: Cohesive strength and separation energy as characteristic parameters of fracture toughness and their relation to micromechanics. Structural Integrity and Durability 1 (2005), 233-241.

[4] Brocks, W.; Cornec, A.; Scheider, I.: Computational Aspects of Nonlinear Fracture Mechanics. In: Milne, I.; Ritchie, R.O.; Karihaloo, B. (Eds.): Comprehensive Structural Integrity - Numerical and Computational Methods. Vol. 3 Oxford: Elsevier, 2003. 127-209. (ISBN: 0-08-043749-4)

[5] Scheider, I.: The Cohesive Model, Foundations and Implementation, 2nd revised edition, Helmholtz Centre Geesthacht, 2006.

[6] Needleman, A.: An analysis of decohesion along an imperfect interface, Int. J. Fract. 42(1990), 21-40.

[7] Tvergaard, V.; Hutchinson, J.W.: The relation between crack growth resistance and fracture process parameters in elastic-plastic solids, J. Mech. Phys. Solids 40 (1992), 1377-1397.

[8] Scheider, I.; Brocks, W.: Simulation of cup-cone fracture using the cohesive zone model. Eng. Fract. Mech. 70(2003), 1943-1961.

[9] Elices, M.; Guinea, G.V.; Gómez, J.; Planas, J.: The cohesive zone model: advantages, limitations and challenges. Eng. Fract. Mech. 69 (2002), 137-163.

[10] ABAQUS Analysis User's Manual (6.11): 33.2.1 Linear constraint equations.

[11] Scheider, I.; Schödel, M.; Brocks, W.; Schönfeld, W.: Crack propagation analyses with CTOA and cohesive model: Comparison and experimental validation. Eng. Fract. Mech. 73 (2006), 252-263.

[12] Brocks, W.; Scheider, I.: Identification of material parameters for structural analyses. Struct. Durab. Health Monit. 161 (2010), 1-24.

[13] Schwalbe, K.-H.: Introduction of δ5 as an operational definition of the CTOD and its practical use. In: Fracture Mechanics, 26th Vol. (eds. W.G. Reuter, J.H. Underwood and J.C. Newman), ASTM STP 1256, American Society for Testing and Materials, 1995, 763-778.

[14] Scheider, I.; Brocks, W.: Residual strength prediction of a complex structure using crack extension analyses. Eng. Fract. Mech.75 (2008), 4001-4017.

[15] ASTM E 1820: Standard test method for measurement of fracture toughness. Annual book of ASTM standards, vol. 03.01. Philadelphia: American Society for Testing and Materials.